

The effect of topography of upper-mantle discontinuities on *SS* precursors

Maria Koroni and Jeannot Trampert

Department of Earth Sciences, Universiteit Utrecht, Heidelberglaan 2, NL-3584 CS Utrecht, The Netherlands. E-mail: m.koroni@uu.nl

Accepted 2015 October 27. Received 2015 October 27; in original form 2015 June 16

SUMMARY

Using the spectral-element method, we explored the effect of topography of upper-mantle discontinuities on the traveltimes of *SS* precursors recorded on transverse component seismograms. The latter are routinely used to infer the topography of mantle transition zone discontinuities. The step from precursory traveltimes to topographic changes is mainly done using linearised ray theory, or sometimes using finite-frequency kernels. We simulated exact seismograms in 1-D and 3-D elastic models of the mantle. In a second simulation, we added topography to the discontinuities. We compared the waveforms obtained with and without topography by cross correlation of the *SS* precursors. Since we did not add noise, the precursors are visible in individual seismograms without the need of stacking. The resulting time anomalies were then converted into topographic variations and compared to the original topographic models. Based on the correlation between initial and inferred models, and provided that ray coverage is good, we found that linearised ray theory gives a relatively good idea on the location of the uplifts and depressions of the discontinuities. It seriously underestimates the amplitude of the topographic variations by a factor ranging between 2 and 7. Real data depend on the 3-D elastic structure and the topography. All studies to date correct for the 3-D elastic effects assuming that the traveltimes can be linearly decomposed into a structure and a discontinuity part. We found a strong non-linearity in this decomposition which cannot be modelled without a fully non-linear inversion for elastic structure and discontinuities simultaneously.

Key words: Body waves; Computational seismology; Wave propagation.

1 INTRODUCTION

The nature of the mantle transition zone (MTZ) discontinuities is still not fully understood, despite their potential importance for understanding the mineralogical and geodynamic state of the mantle, for example, Morgan & Shearer (1993). The systematic investigation of the topography of the discontinuities at around 410 km depth, henceforth denoted as ‘410’ and at around 660 km depth, referred to as ‘660’, is conducted with a variety of techniques. The most effective approach has been the use of precursors of surface reflected phases such as *SS*, and to a lesser extent *PP* (e.g. Shearer 1991; Shearer & Masters 1992; Shearer 1993; Vasco *et al.* 1995; Estabrook & Kind 1996; Flanagan & Shearer 1998, 1999; Shearer *et al.* 1999; Shearer 2000; Gu & Dziewonski 2002; Deuss & Woodhouse 2002; Gu *et al.* 2003; Schmerr & Garnero 2006, 2007; Deuss 2007, 2009; Lawrence & Shearer 2008; Houser *et al.* 2008; Thomas & Billen 2009; Lessing *et al.* 2014). These data are particularly attractive because their main sensitivity is concentrated near their bounce points (or midpoints), which are halfway between source and receiver, for a source at the surface. They also provide a good global coverage (e.g. Deuss 2009).

The traveltime differences between main and precursory phases, together with linearised ray theory (Fig. 1), have allowed scientists

to produce global maps of the topography of MTZ discontinuities. Other studies have used receiver functions to analyse *Ps* and *Sp* conversions to determine the topography of the MTZ discontinuities using regional and global data, (e.g. Paulssen 1988; Shearer 1991; Chevrot *et al.* 1999; Tonegawa *et al.* 2005; Lawrence & Shearer 2006; Andrews & Deuss 2008; Tauzin *et al.* 2008; Eagar *et al.* 2010; Tauzin *et al.* 2013). The receiver function method is predominantly sensitive to structure beneath the recording station; therefore, it can provide detailed maps of topography of the ‘410’ and ‘660’ mainly in continental regions.

Although many studies have been published, the results for topography of the MTZ discontinuities show considerable dissimilarities. Most differences seem to arise from the employed method of stacking and from automating the procedure of picking and aligning reference phases (e.g. Houser *et al.* 2008; Schultz & Gu 2013; Zheng *et al.* 2015). The majority of studies use long-period data together with linearised ray theory to map the large-scale topographic structure (Flanagan & Shearer 1999; Houser *et al.* 2008). The main limitation of ray theory is that it neglects the full sensitivity of the data to the discontinuities by assuming that this is mainly concentrated at the bounce point. Theoretical studies of the sensitivity of precursors showed that the complexities related to the Fresnel zone of the *SS* underside reflections can lead to underestimations

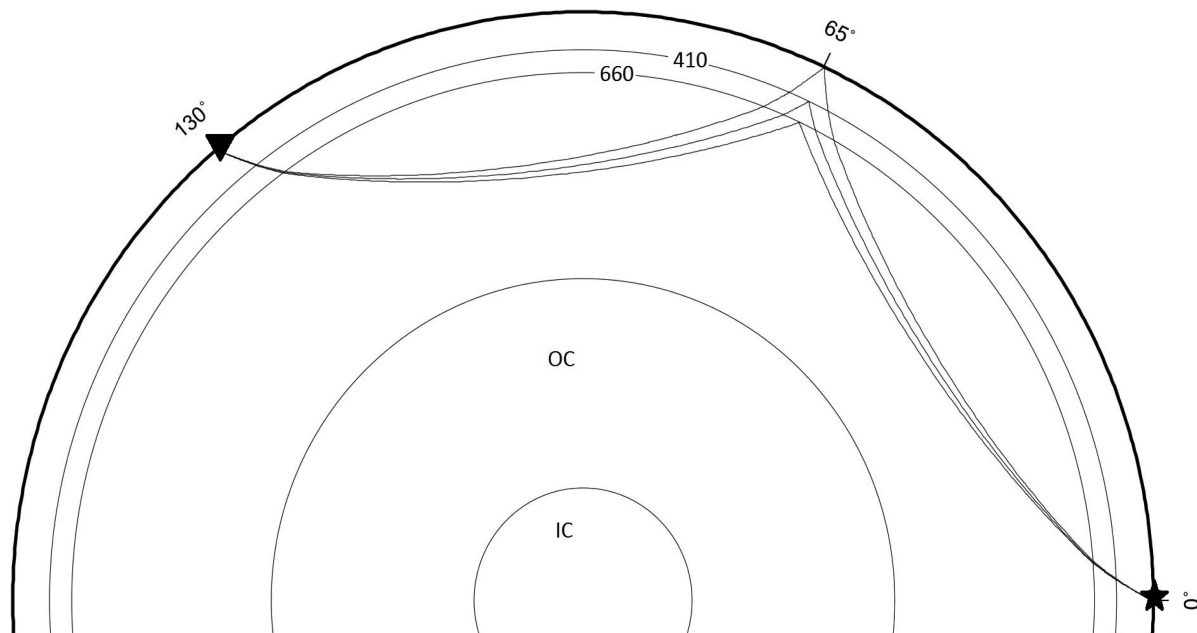


Figure 1. Ray paths of the *SS* phase and its precursors, that is, *S410S* and *S660S*, at an epicentral distance equal to 130° . The black triangle denotes the receiver and the black star the source. *OC* denotes outer core and *IC* inner core.

of the depth variations in the discontinuities (e.g. Chaljub & Taran-tola 1997; Neele *et al.* 1997; Zhao & Chevrot 2003). Lawrence & Shearer (2008) were the first to use finite-frequency kernels to invert the underside reflection data and obtained better resolved images of the topography (compared to previous studies).

The traveltimes of the *SS* precursors do not only depend on the depths of the discontinuities, but also on the 3-D wave speed structure of the mantle through which these phases travel. Bai *et al.* (2012) investigated the validity of ray theory to correct for the effect of velocity heterogeneity on the traveltimes of *SS* precursors. They computed synthetic seismograms for three differently damped versions of the 3-D isotropic model S20RTS (Ritsema *et al.* 1999) by using a spectral-element method. Their results show that ray-theoretical corrections for 3-D mantle wave speeds only account for about 50 per cent of the observed anomalies. They conclude, similar to previous studies, that finite-frequency approaches are necessary to remove the imprint of 3-D wave speed mantle structure.

In this study, we investigate for the first time the reliability of linearised ray theory for converting (suitably corrected) *SS* precursors into depths of MTZ discontinuities. We calculated exact synthetic seismograms using a spectral-element method, where we explicitly included topography of mantle discontinuities. Besides the topography, we also used various 1-D and 3-D elastic models of the mantle. The topography models for the ‘410’ and ‘660’ are taken from the study of Meier *et al.* (2009) and the elastic models are PREM (Dziewoński & Anderson 1981) and S20RTS (Ritsema *et al.* 1999). The simulations were carried out using SPEC-FEM3D_GLOBE (Komatitsch & Vilotte 1998; Komatitsch & Tromp 1999, 2002a,b).

2 DATA AND METHODS

2.1 Synthetic data

Working with real data entails many complexities which we seek to avoid in this synthetic experiment. The aim is to understand if seismology is in principle able to recover discontinuity topography

using existing techniques. This aim is best served by keeping the experiment as simple as possible. We generated noise-free, exact synthetic seismograms in elastic 1-D and 3-D models for a random, uniform station distribution using the spectral-element code developed by Komatitsch & Tromp (2002a,b). SPEC-FEM3D_GLOBE is distributed with the model S362ANI (Kustowski *et al.* 2008) which includes topography of the ‘410’ and ‘660’ discontinuities. We modified the code in such a way that any 3-D crustal or mantle model and any discontinuity model of the Moho, ‘410’, ‘660’ and CMB, all parametrised in spherical harmonics, can be used in any combination. We computed seismograms using two elastic Earth models, PREM (Dziewoński & Anderson 1981) and S20RTS (Ritsema *et al.* 1999) together with CRUST2.0 (Bassin *et al.* 2000) without topography of the mantle discontinuities. We then switched the discontinuity models on using the same two elastic models. The topography models we used were derived by Meier *et al.* (2009) and contain lateral variations up to spherical harmonic degree 8. The topography models are plotted in Figs 2 and 3. The exact nature of the models is not important here, but the reader should keep in mind that the models are relatively smooth, that is, spherical harmonic degree ≤ 8 . Our intention is to establish if imaging the topography is feasible using existing linearised ray-theoretical techniques. All other features of SPEC-FEM3D_GLOBE (attenuation, rotation, ellipticity, gravity and surface topography) are switched off as they would generate signal we do not wish to analyse here, see Komatitsch & Tromp (2002a,b).

Although the use of *SS* precursors results in a fairly global distribution of bounce points, their distribution is far from uniform (Deuss 2009). This uneven distribution could bias the inferences on topography of the MTZ discontinuities. We did not want to complicate our conclusions due to an irregular distribution of bounce points and thus we generated a set of seismic stations and events to achieve a uniform random distribution of *SS* bounce points over the sphere. 12 events were regularly spaced every 30° along the equator. The event depth is 20 km and the mechanism is a pure strike-slip with an event magnitude of 7.9, which should favour a strong *SS* radiation. The source time function is a Gaussian of

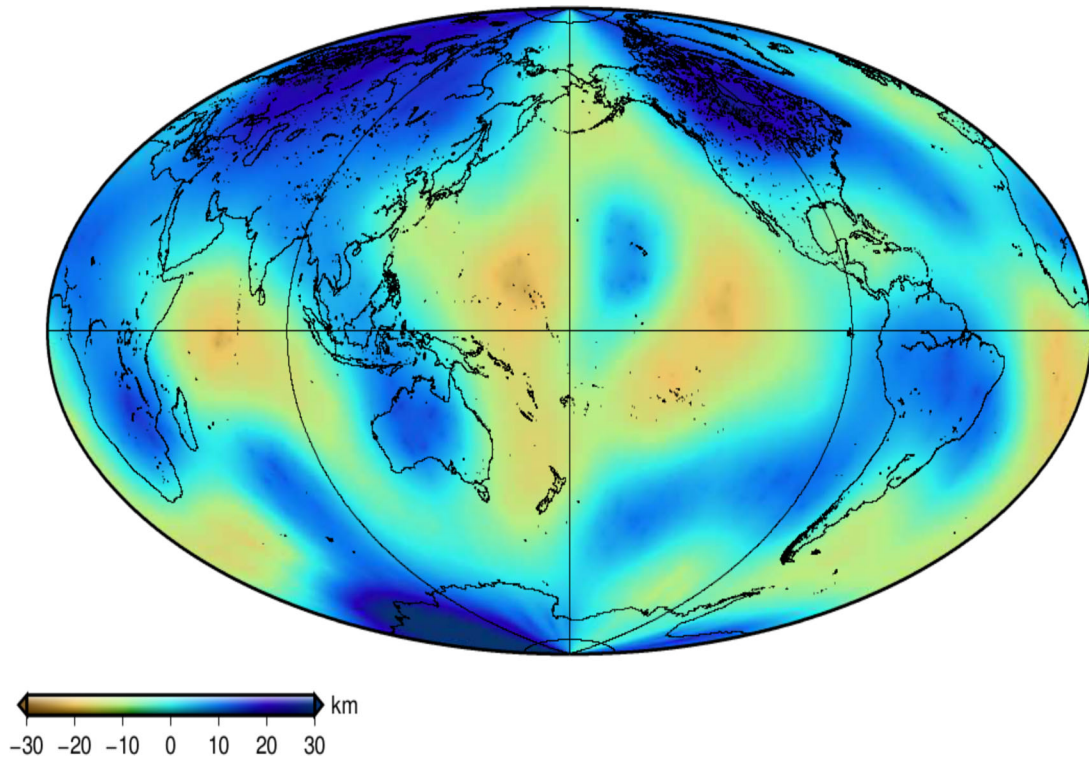


Figure 2. Model of the '410' discontinuity used in this study (Meier *et al.* 2009). Represented are deviations from the reference depth. Yellow areas indicate uplifts of the discontinuity whereas blue areas correspond to depressions.

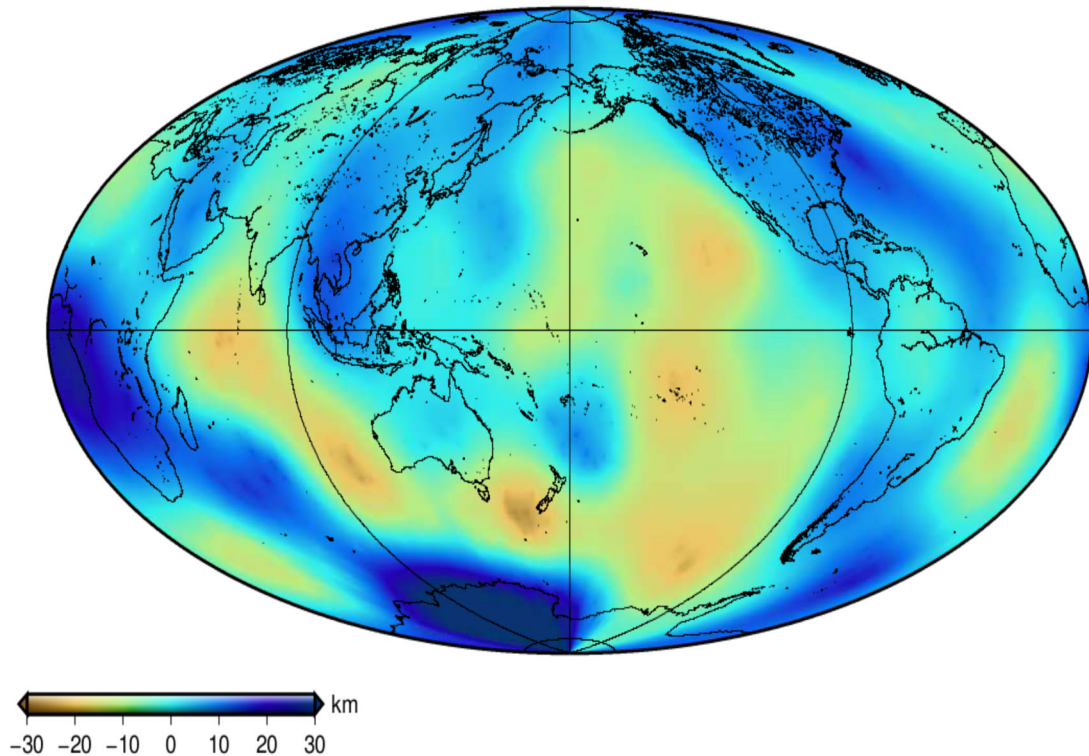


Figure 3. Same as Fig. 2, but for the '660'.

half-width 30 s. The stations were randomly chosen in the distance range of 110° – 160° to avoid interference by surface multiples or topside reflections (e.g. *Ss670s*, *Ss400s*) and depth phases (e.g. *Sc-SScS*). In this way, we create the uniform distribution of midpoints which can be seen in Fig. 4.

We generated in total 6211 1-hr long transverse component seismograms for each Earth model. Fig. 5 shows a record section for a simulation using S20RTS (and CRUST2.0) plus the MTZ topography models. The data are available via http://www.geo.uu.nl/~jeannot/My_web_pages/Downloads.html.

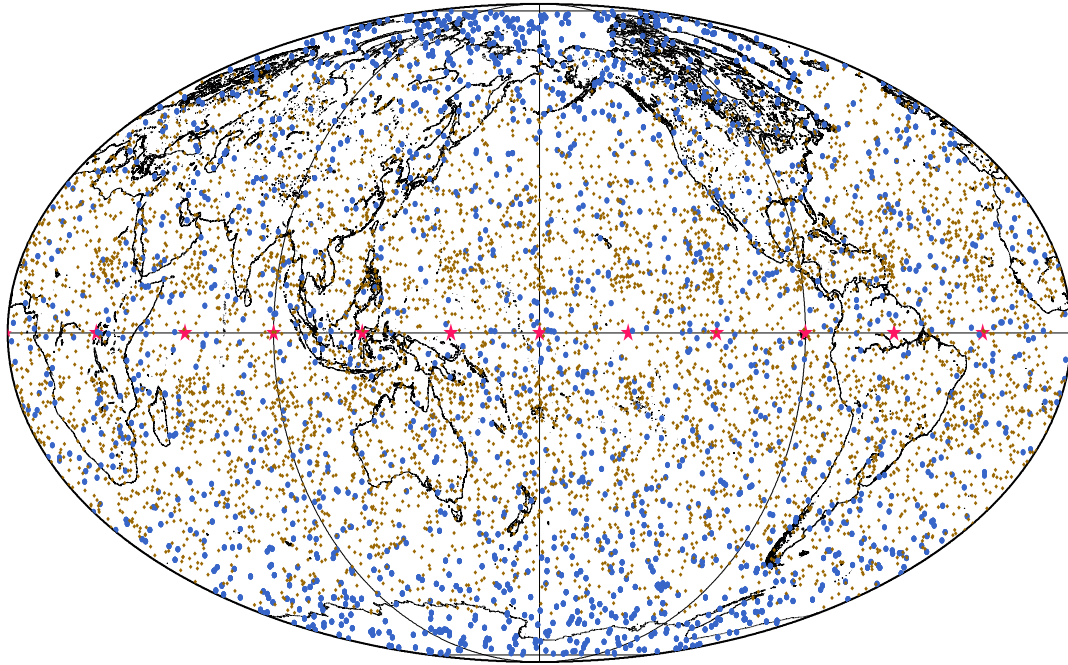


Figure 4. Virtual events (red stars) and randomly generated stations (brown rhombi). The midpoints are shown by blue dots. The uniform coverage of the bounce points is ideal for an *SS* precursor study.

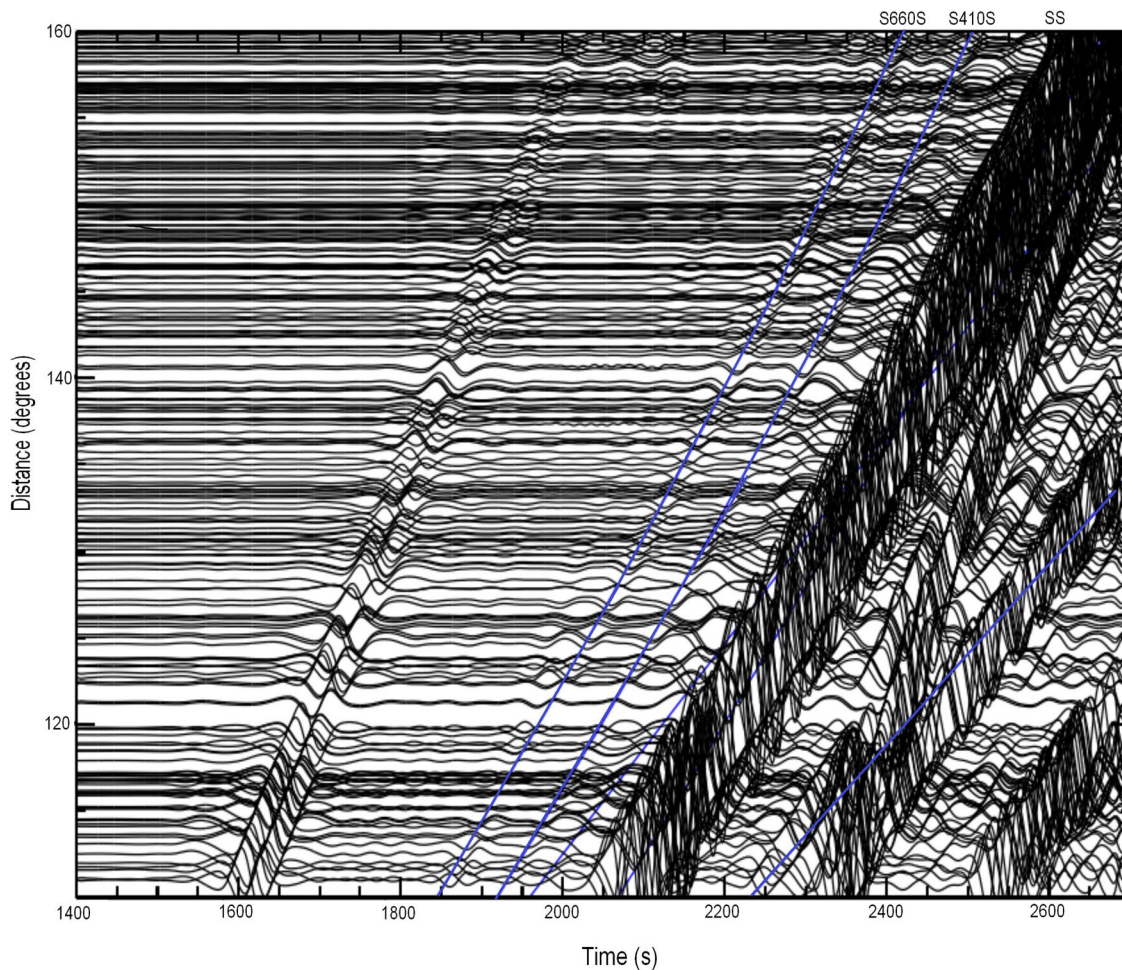


Figure 5. Record section showing the *SS* phase and its precursors in the epicentral distance range 110° – 160° . The blue lines indicate the theoretical traveltime curves of these phases. The seismograms correspond to the model S20RTS+CRUST2.0 plus MTZ topography.

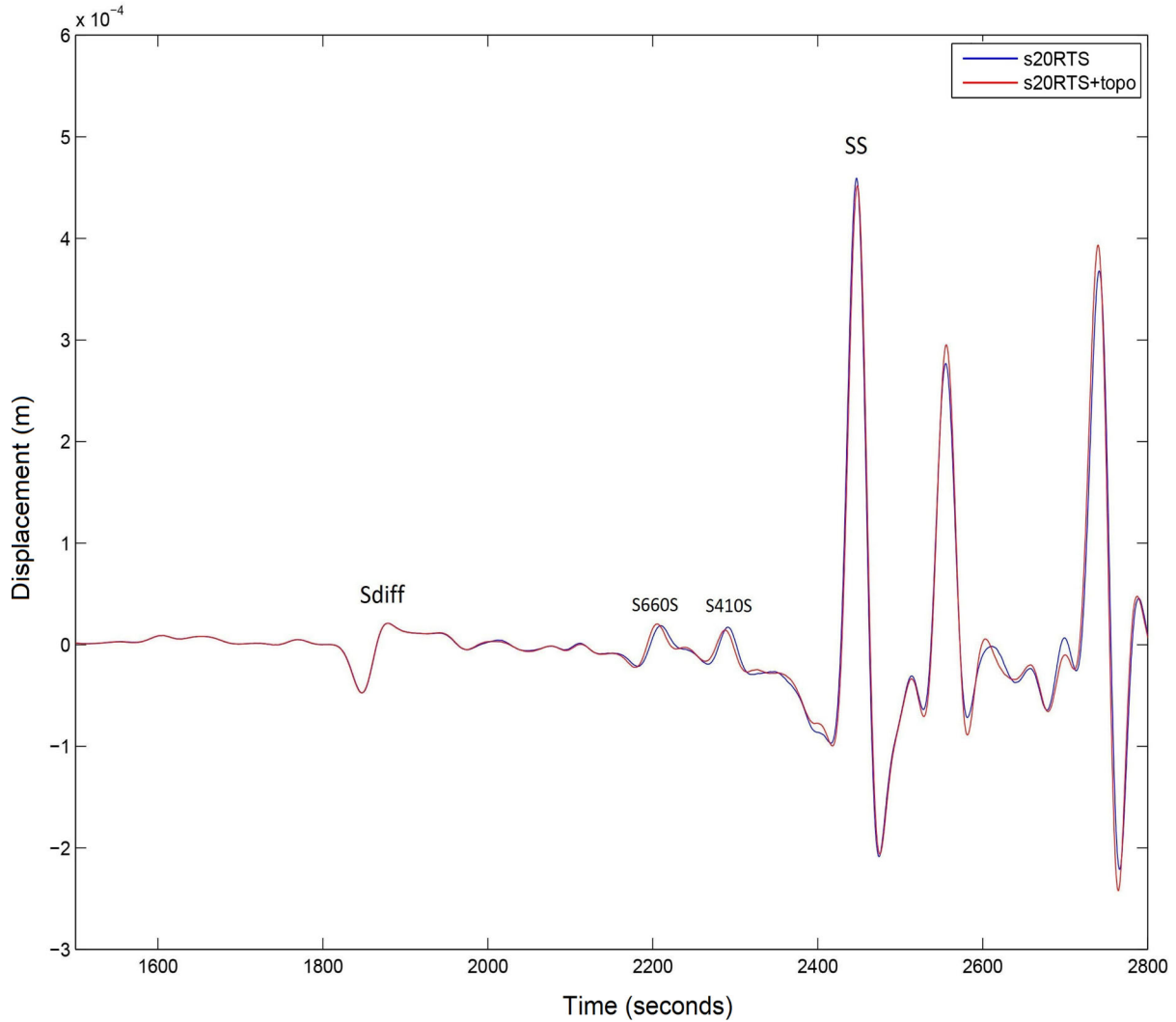


Figure 6. The change on the transverse component of seismogram number 4119 caused by the addition of topography. The epicentral distance is 140 deg. The red line corresponds to a seismogram in model S20RTS+CRUST2.0 with topography of the ‘410’ and ‘660’, whereas the blue line is the signal for the same 3-D model without topography.

2.2 Methods

As shown on the record section in Fig. 5, the *SS* precursors can be identified on individual seismograms. We therefore did not resort to stacking as is done in most *SS* precursor studies (e.g. Deuss 2009; Bai *et al.* 2012). To measure the delay time caused by the topography, we performed a simple cross correlation between suitably cut waveforms with and without topography. The traveltime anomaly δt of the precursor is found at the maximum of the cross correlation. The maximum value informs us on how similar the waveforms are, which is important for quality control. For each path, we measure:

$$\delta t = t_{SdS}^{X+topo} - t_{SdS}^X \quad (1)$$

where X stands for PREM or S20RTS+CRUST2.0 and d is the reference depth of the discontinuity, that is, ‘410’ or ‘660’. In the linearised ray-theoretical approximation, this delay time is linked to the depth perturbation of the discontinuity δh at the bounce point via:

$$\delta t = -2 \frac{\delta h}{V_s} \cos i \quad (2)$$

where V_s is the underside shear wave speed and i the incidence angle at the bounce point. It is simply the two-way traveltime of the ray in the uplifted or depressed part of the topography. We used PREM traveltimes, obtained by the TauP software (Crotwell *et al.* 1999), to identify the *SS* precursors. There are notable time-shifts between seismograms with and without topography (Fig. 6). Close-ups of the *SS* precursors can be seen in Figs 7–9. The *SdS* phases are isolated by cutting a cosine taper data window of 40 s on either side of the PREM precursor arrival in all seismograms. The 3-D mantle structure and/or topography should produce a delay up to approximately 10–15 s; thus, we are confident that we can use the PREM arrival time window on all the seismograms. In order for the cross correlation method to work, the two waveforms need to be similar. For this reason, we eliminated picks where the aligned waveforms had a correlation of less than 0.9.

The results are analysed in three different ways. Since the depth variation is known at each bounce point, we converted it into ray-theoretical traveltime anomalies using eq. (2). We then plotted the measured delay times against the ray-theoretical ones. If ray theory can reliably be used to infer the depths of the discontinuities, the points should fall close to a line of slope one. We do not expect

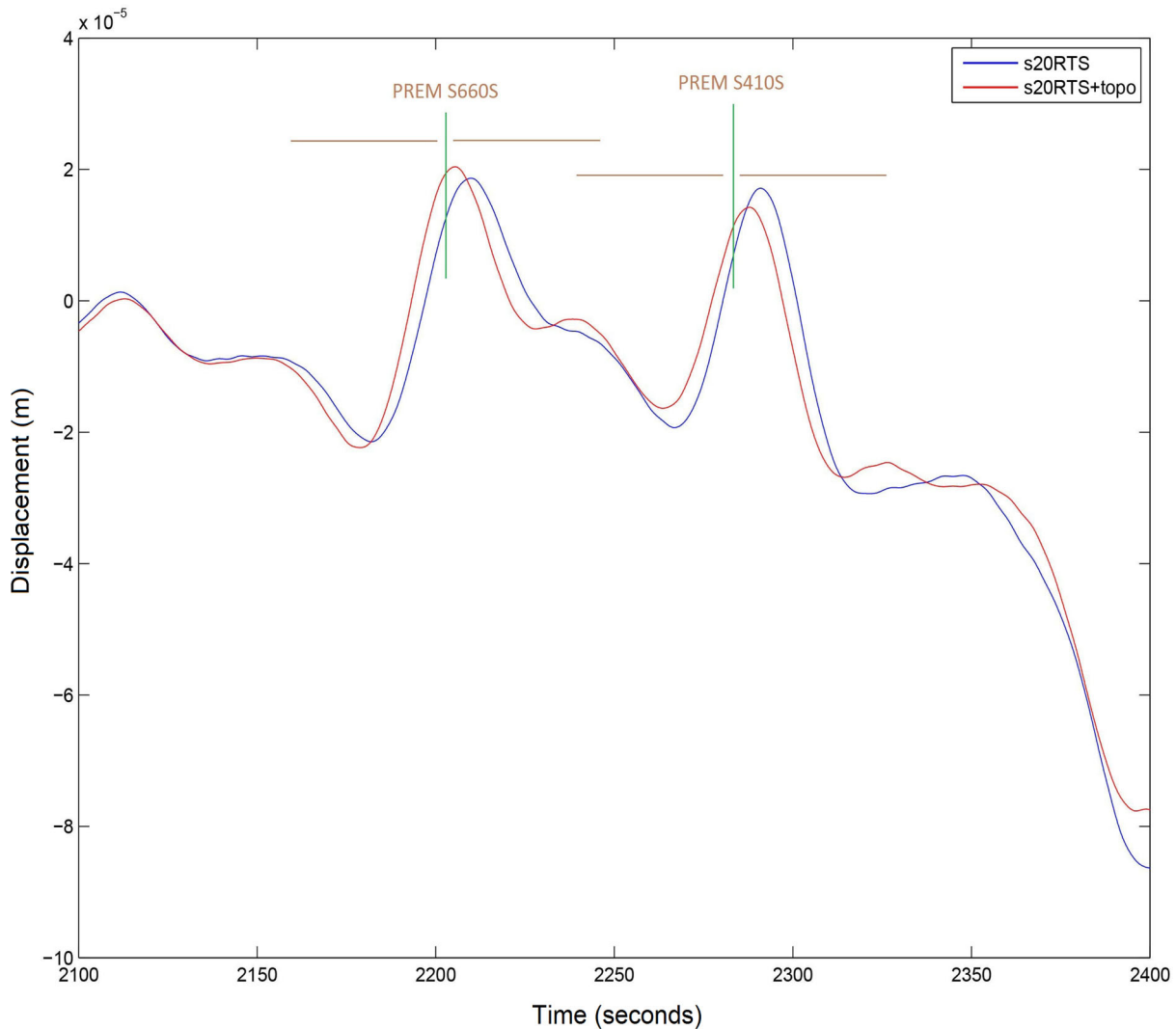


Figure 7. Same as in Fig. 6, now zooming on the *SdS* precursors. The green vertical lines indicate the predicted PREM arrivals, the brown horizontal lines show 40 s on either side of the PREM arrival defining the window for cross correlation. The cross correlation measurement at the *S400S* is 1.94 s while the ray-theoretical prediction is 0.66. At the *S660S*, the cross correlation is -3.55 while the ray-theoretical prediction is -4.38 . In this case there is a close agreement between the cross correlation and the ray-theoretical prediction (Δt is small).

a perfect line and in order to estimate the amount of scatter, we analysed the histograms of the difference in traveltime anomalies defined as:

$$\Delta t = \delta t^{cc} - \delta t^{rt} \quad (3)$$

where ‘*cc*’ stands for the cross correlation measurement and ‘*rt*’ the ray-theoretical prediction using the topography at the bounce point using eq. (2). A more quantitative comparison between full input models of the discontinuities and the measured traveltime anomalies is achieved by converting the measured time delays into ray-theoretical depth anomalies using again eq. (2). Next, we expanded the obtained ray-theoretical depth perturbations, $\delta h_{rt} = \frac{-\delta t^{cc} V_s}{2 \cos i}$, into spherical harmonics and compared them to the original topography models. More specifically, we analysed their cross correlation and root-mean-square (rms) amplitude ratio as a function of spherical harmonic degree. All results are presented in the following section.

3 RESULTS

We automatically measured delay times from *SdS* waveforms corresponding to models with and without topography. They are presented in scatter plots against ray-theoretical delay times calculated from the input topography at the bounce points. For the case of a 1-D elastic background model, the results can be seen in Figs 10 and 11. From these scatter plots, we can infer two things. There is clearly a positive correlation between the measured and predicted delay times and the slope is significantly different from one. This means that we can infer the sign of the topography with some degree of confidence, but not its amplitude. In the ideal case, all points would fall on a line with slope one. A linear least-squares fit of the points in Fig. 10 gives a slope of about 2.5. This number should be treated with care as the slope is influenced by outliers. The scatter could be due to measurement errors, although this is not likely as we use noise-free synthetics and a correlation threshold of 0.9 for the measurements and non-ray-theoretical effects. The latter is most likely and best seen in histograms of the difference between

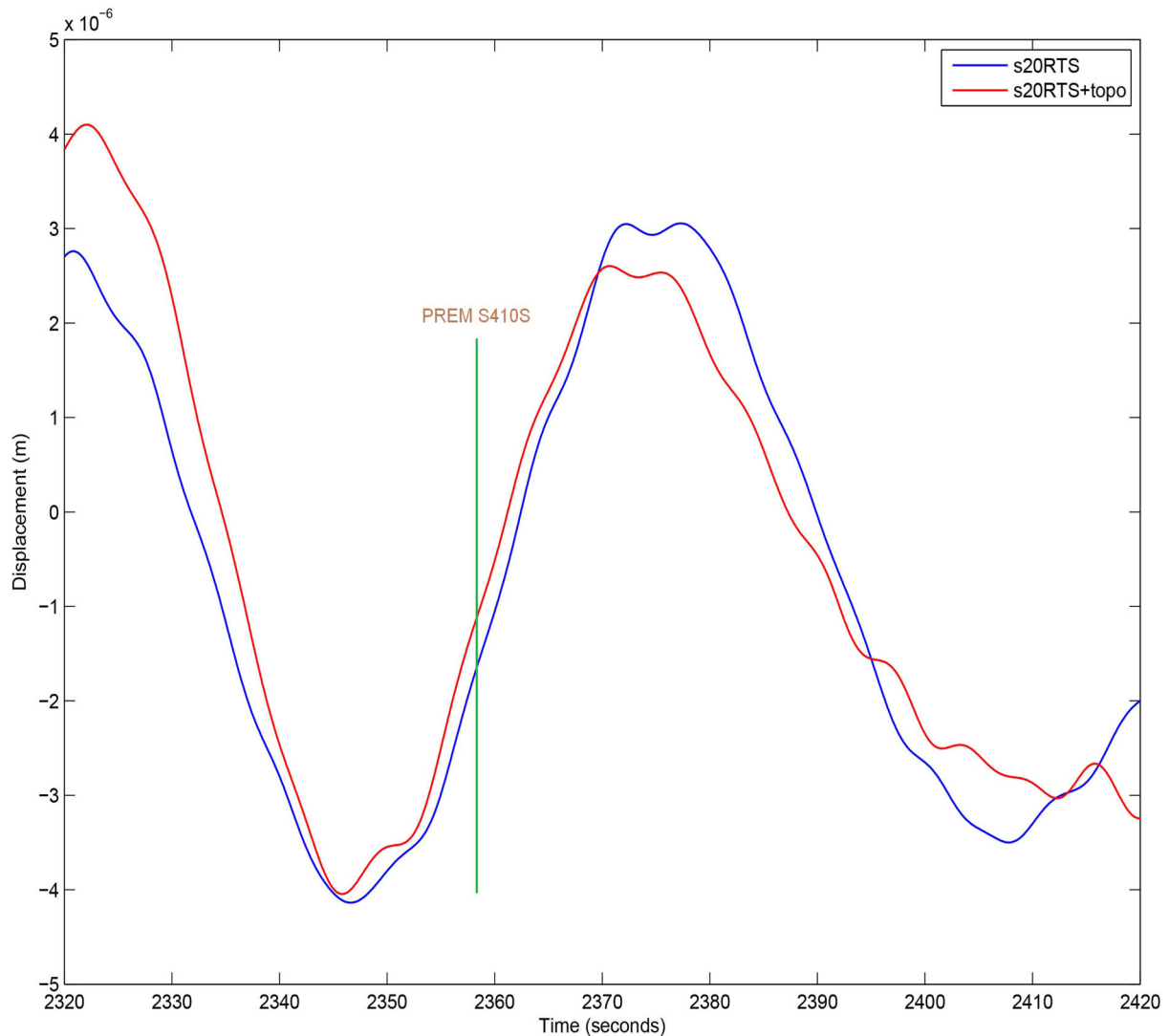


Figure 8. Zoom on the *S410S* precursor in a 3-D background. The seismogram number is 3780. The epicentral distance is 151° . For the *S410S*, the cross correlation measurement is 1.45 while the ray-theoretical prediction at the same point is -17.60 s. This is an example of large Δt .

measured and predicted delay times, Δt . While the measured delay times due to topography on the ‘410’ show a normal distribution, Δt is bi-modal (Fig. 12). If the predicted delay times were simply a scaled version of the measured ones (with some noise), they would also be normally distributed, only broader due to a slope steeper than one. The slope for the data from the ‘660’ discontinuity is less steep indicating that we get a better idea on the amplitude in this case (Fig. 11). Regarding the ‘660’ case, the histogram of Δt does not show the bimodality (Fig. 13) as seen for ‘410’ (Fig. 12).

Very similar qualitative conclusions can be drawn in a 3-D elastic background model (Figs 14 and 15). This means that if we are able to correct the measurements for the 3-D elastic effects (see a discussion on this in Bai *et al.* 2012), we should in principle be able to do similarly well as in the 1-D case (i.e. get the sign of the topography but not its amplitude).

To be more quantitative about inferences on topography, it is most instructive to convert the measured delay times into ray-theoretical depth perturbations using eq. (2), expand them into spherical harmonics and compare with the input topography model. An example is shown in Fig. 16, where we see what we already inferred from the scatter plots: the positions of the uplifts and depressions are cor-

rect, but with subdued amplitudes. We then expanded our inferred model up to degree 20 with a smoothness constraint (Laplacian with weight 0.01) to avoid spectral leakage (Trampert & Snieder 1996), but only show results up to degree 8. We also do not show degree 0, which was not present in the input model. The variance reduction of the models as well as the number of data used are shown in Table 1. Bear in mind that we made automatic measurements with a strong constraint on the similarity of the two waveforms for cross correlations. This results in discarding a fair amount of measurements because many waveforms became too distorted by the topography. For delay times in 1-D background models, we can explain about 60–72 per cent of the variance whereas in 3-D background models only about 50–56 per cent. The correlation (Fig. 17) confirms what we saw in the scatter plots: the ray-theoretical estimates map the sign of the topography very well. The rms amplitude ratio (Fig. 18) shows that we considerably underestimate the magnitude of the topography. We see two interesting points: the amplitude of the ‘660’ topography is better recovered than that of ‘410’ and topography in a 1-D background model is better recovered than that in a 3-D background model. The amplitude ratios are qualitatively in agreement with the slopes seen on the scatter plots, but are more robust as they

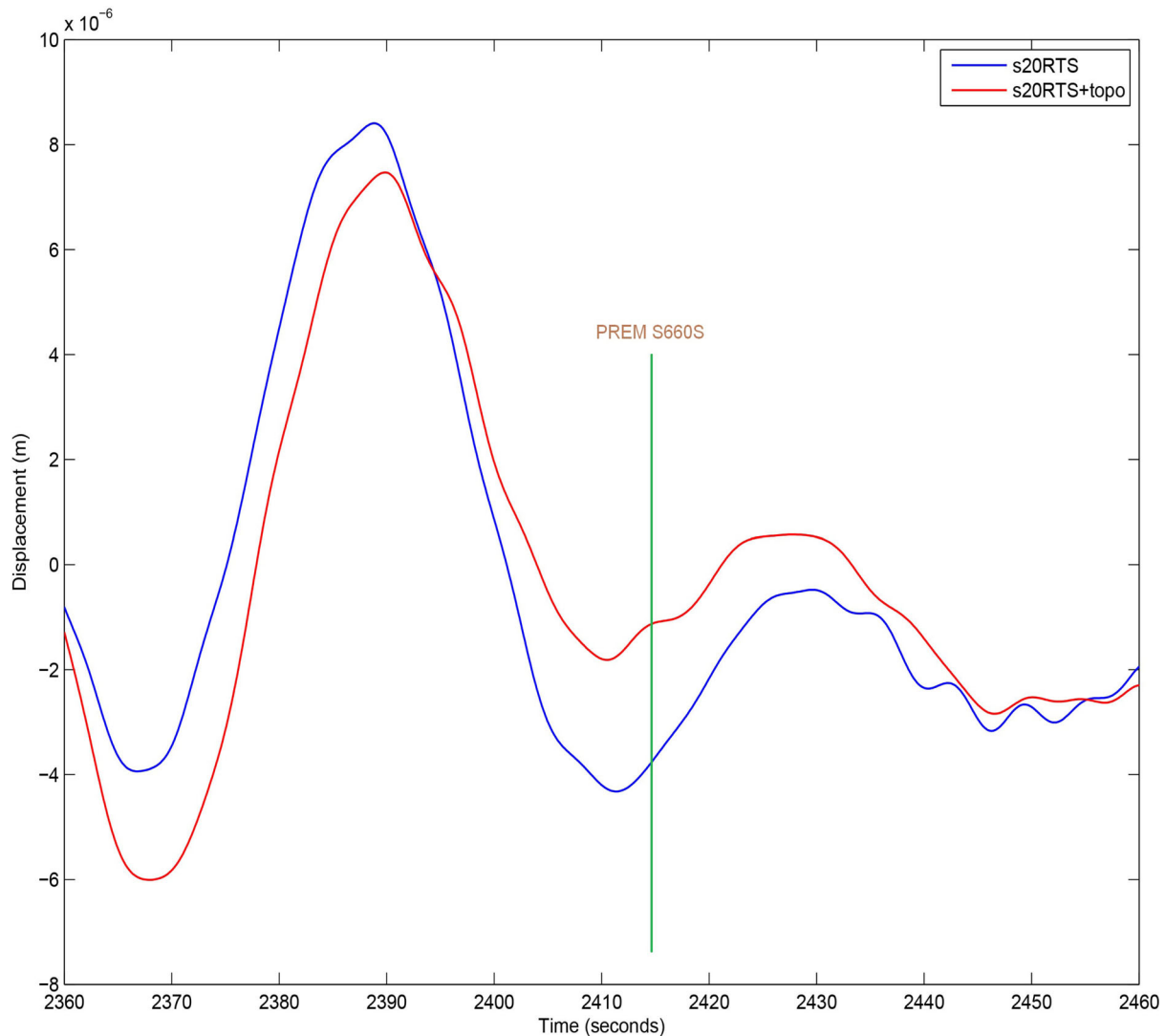


Figure 9. Zoom on the *S660S* precursor in 3-D background. Seismogram number is 6013. The epicentral distance is 154° . For the *S660S* the cross correlation measurement is -0.16 while the ray-theoretical prediction is -15.94 s. This is another example of large Δt .

are less influenced by outliers as the least-squares regression lines. We will come back to these points in the discussion.

4 DISCUSSION

We would like to stress several points from the analysis of the *SS* precursor data. The less steep slope in the scatter plots corresponding to the ‘660’ discontinuity means that the amplitude of the ‘660’ topographic variation can be better resolved than that of the ‘410’ using ray theory. The likely reason is that the seismic waveforms interact with the ‘660’ and are therefore distorted when reaching the ‘410’. We investigated the case of only adding a topography model for the ‘410’ discontinuity. The slope seen in the scatter plots is now considerably less steep than when a ‘660’ is also present. This confirms that the presence of the ‘660’ influences the waveforms corresponding to the ‘410’ precursors considerably. The complication of the data for ‘410’ compared to those for the ‘660’ is best seen in the histograms of Δt . For the ‘660’ they resemble a scaled version of the measurements δt^{cc} (Fig. 13), whereas for the ‘410’ they are bimodal (Fig. 12). This implies that the delay times calculated

by ray theory are not just a scaled version of the measured ones. There could be measurement noise of course, but we used strict quality controls for the measurements. The most likely explanation is that ray theory does not capture the wave propagation effects of the precursors correctly. We should therefore suspect that current models of the ‘410’ topography, inferred from *SS* precursors, are less robust than the existing ‘660’ topography models.

Another interesting point is that the measurements in the 1-D elastic model show less amplitude loss compared to those in the 3-D models. A look at Fig. 18 shows that linearised ray theory explains the data better in 1-D than in 3-D elastic background models. This indicates that the 3-D mantle structure further complicates the interpretation of topography of the discontinuities. This has been known for some time and thus researchers tried to make 3-D corrections, a discussion on which can be found in Bai *et al.* (2012). Our data additionally show, that even if the correction is perfect, the amplitude of topography will be more severely underestimated in a 3-D background model.

Chaljub & Tarantola (1997) showed that the amplitude of uplifts of the ‘660’ should be better retrieved than those for depressions. We tested this conclusion by calculating correlations and amplitude

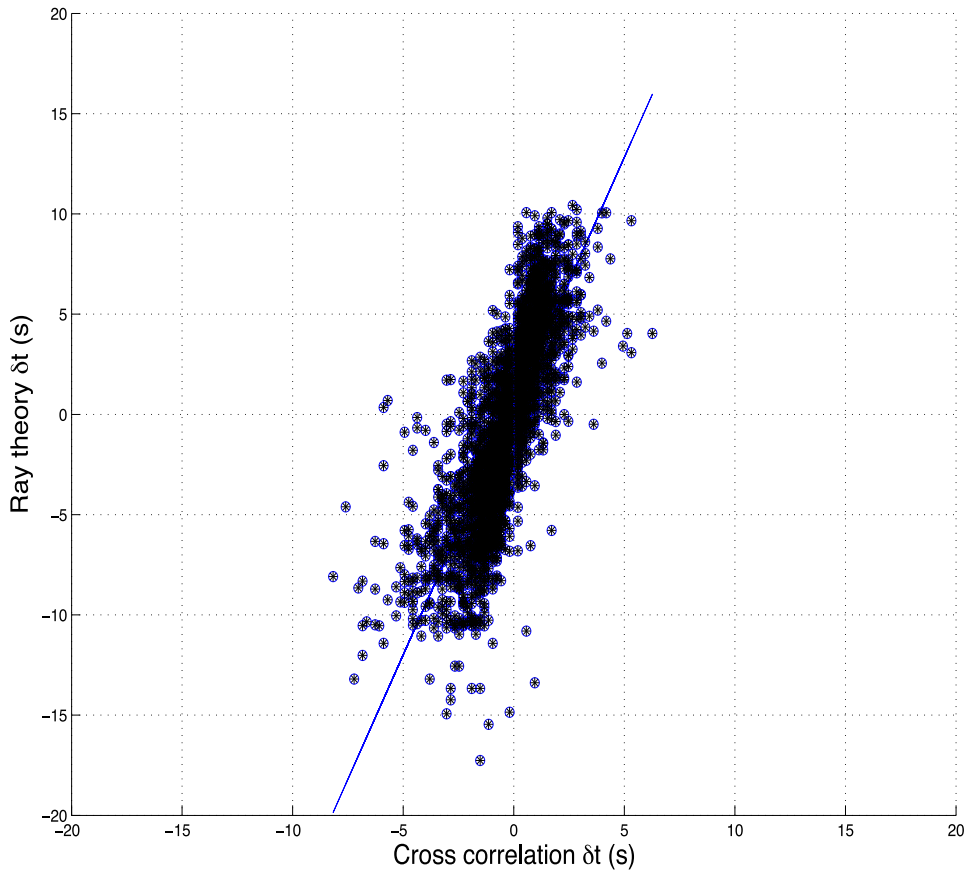


Figure 10. Scatter plot dt^{cc} versus dt^r for S410S in PREM as a background model.

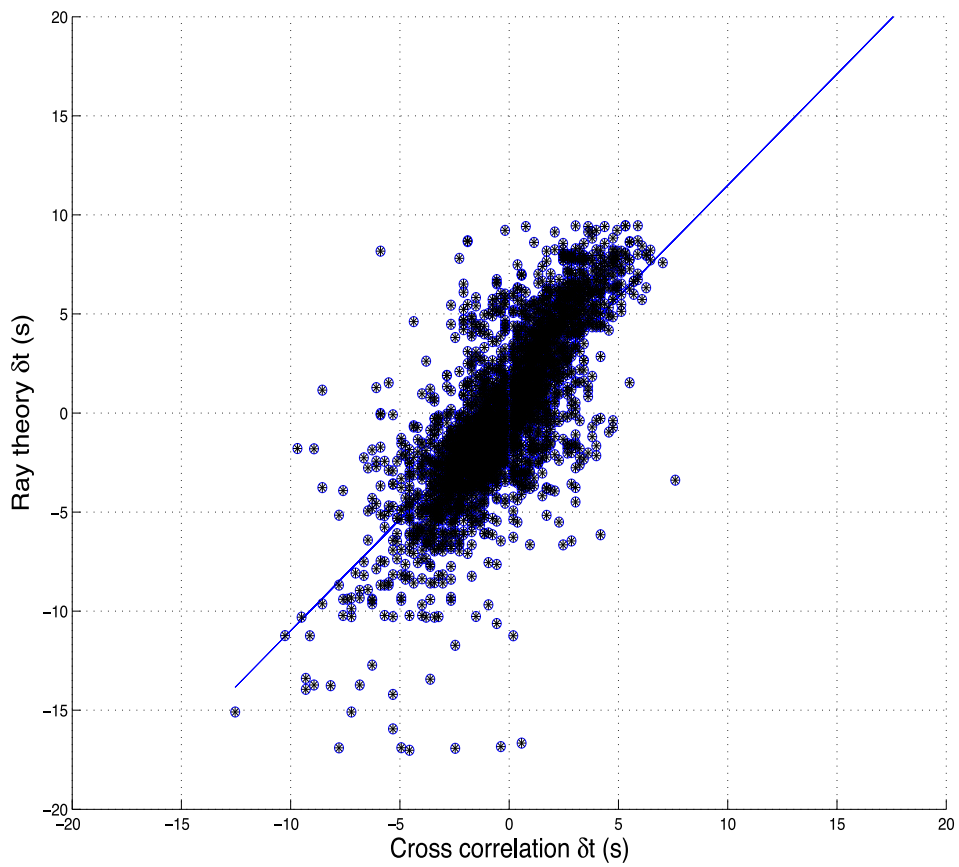


Figure 11. Same as Fig. 10, but for the S660S precursor.

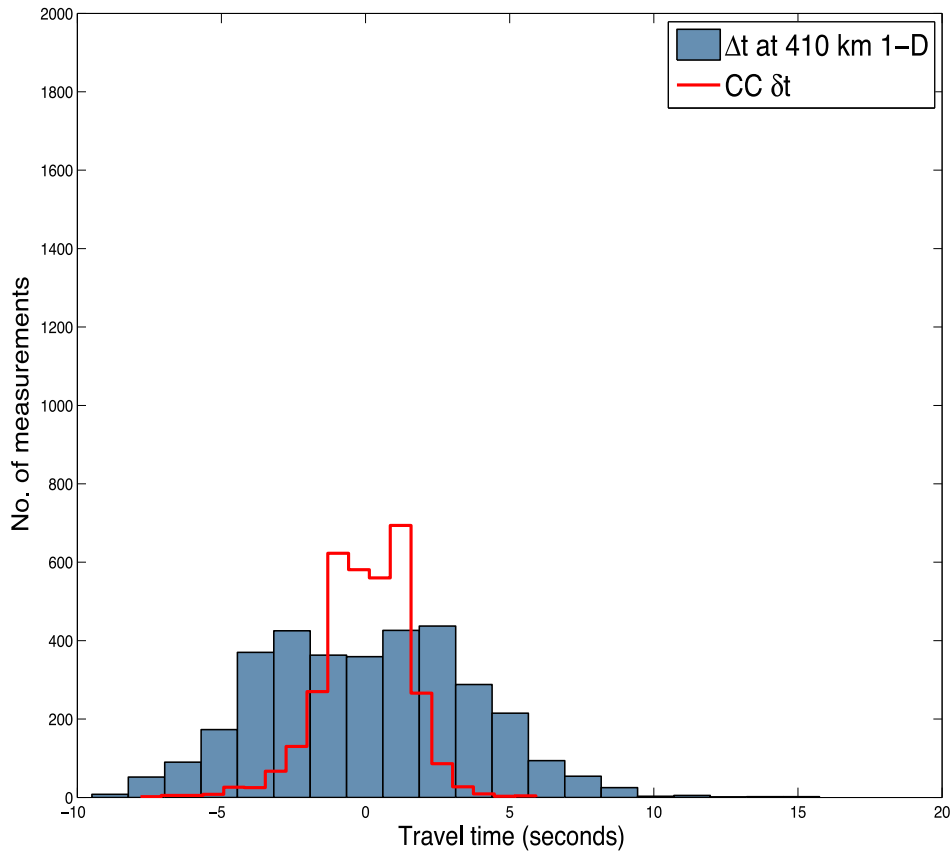


Figure 12. Histogram of the difference in traveltime delays Δt (blue bars) and the measured delay times δt^{CC} (red line) for *S410S* in PREM as a background model.

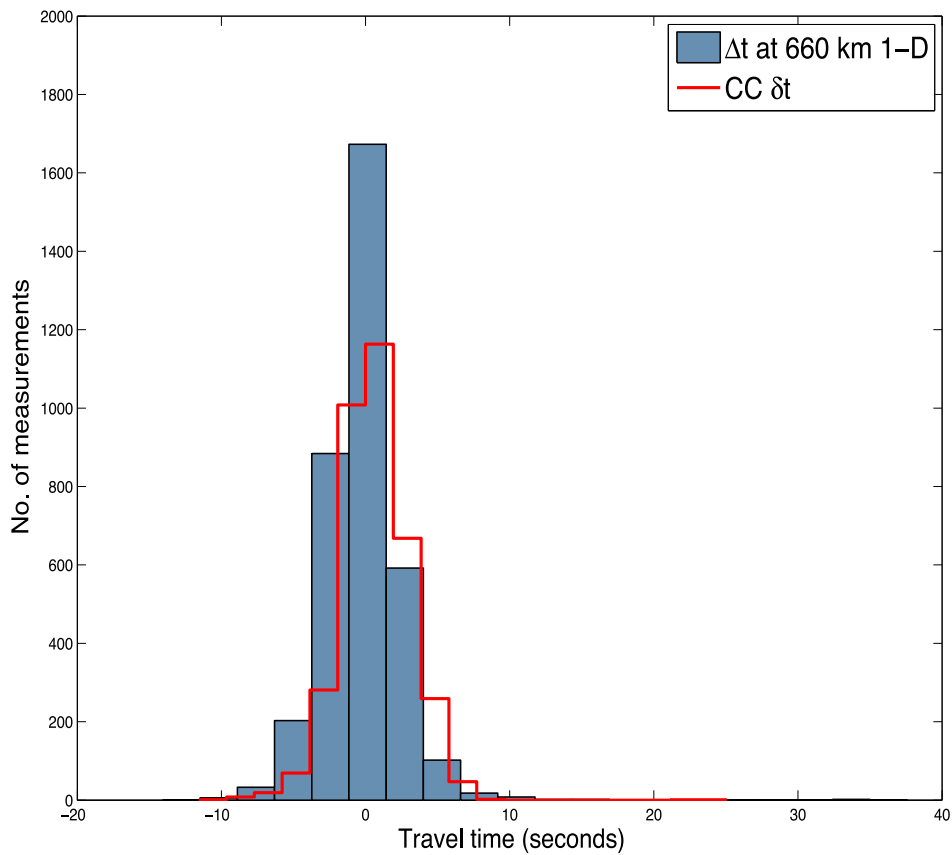


Figure 13. Same as Fig. 12, but for the *S660S* precursor.

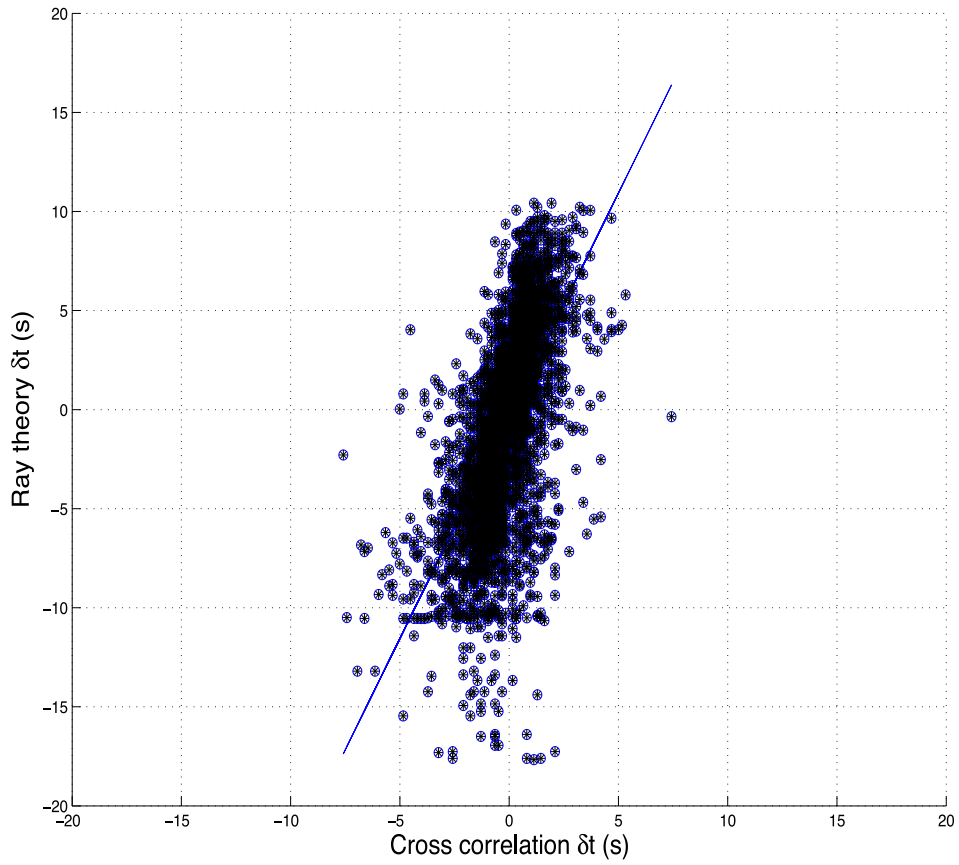


Figure 14. Scatter plot dt^{cc} versus dt^r for S410S in S20RTS+CRUST2.0 as a background model.

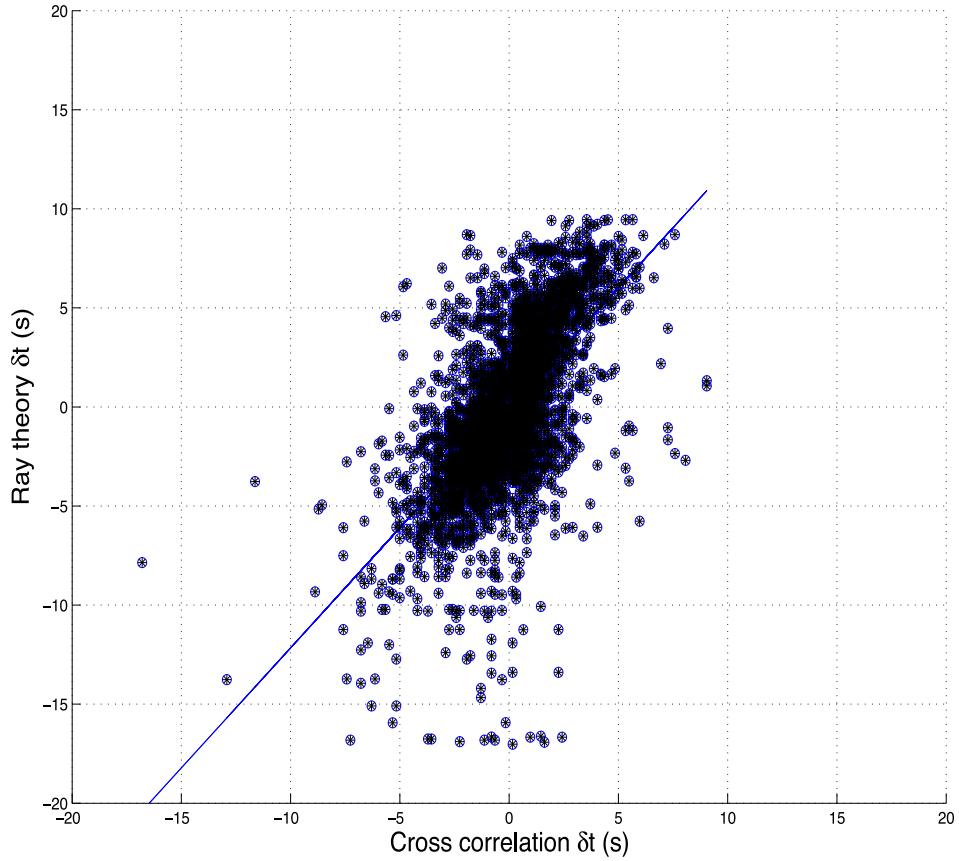


Figure 15. Same as Fig. 14, but for the S660S precursor.

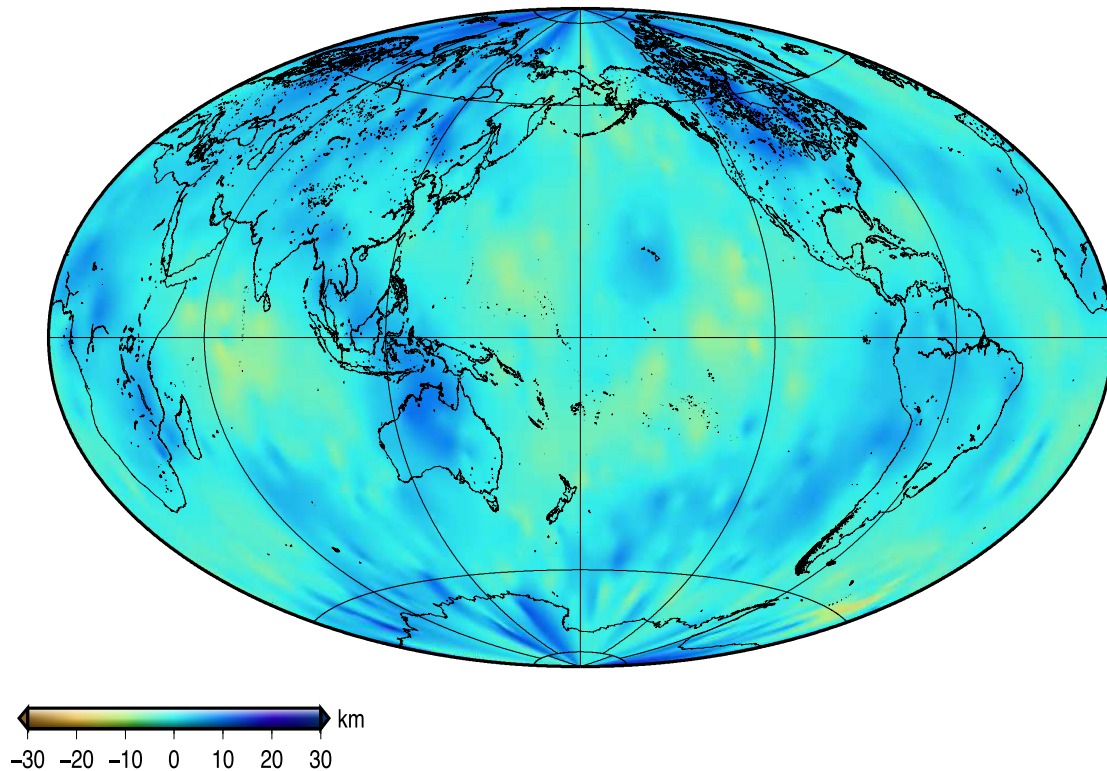


Figure 16. Inferred topography of the ‘410’ at the bounce points from the cross correlation measurements in a PREM background. Note the amplitude loss compared to the initial topography model shown in Fig. 2.

Table 1. Unexplained variance reduction and number of measurements when expanding the ray-theoretical topography predictions into spherical harmonics.

Data set	Unexplained variance per cent	Number of data points
410 _{1-D}	28.71	3392
660 _{1-D}	37.41	3528
410 _{3-D}	51.01	3966
660 _{3-D}	44.97	4158

ratios for negative as well as positive perturbations of the input topography model. We found that in a 1-D background model, the correlation for negative and positive depth perturbations is 0.89 and 0.69, respectively. The amplitude ratios for uplifts (negative depth perturbations) is 2.35 compared to 2.85 for depressions. For the ‘410’, the correlations are 0.93 and 0.79 and the amplitude ratios are 4.59 and 3.21 for uplifts and depressions, respectively. We confirm a clear difference between the quality of the retrieved uplifts and depressions. Our findings are different from those of Chaljub & Tarantola (1997), but our topographic models are multiscale, whereas theirs contained a unique perturbation of fixed length scale.

It is worth remembering that all our simulations were for a uniform distribution of bounce points. Retrieval of topography could worsen if their distribution is not uniform as seen in studies dealing with real data (Deuss 2009) and influence our conclusion of a good correlation between input and inferred model as seen in Fig. 17.

We already mentioned that the time residual depends at the same time on the 3-D elastic structure and the topography of the discontinuity. Most studies attempt to correct for the 3-D effects by correcting the residuals using some 3-D tomographic model (e.g. Gu & Dziewonski 2002; Chambers *et al.* 2005; Lawrence & Shearer 2008) or invert simultaneously for mantle velocity and topography (e.g. Gu *et al.* 2003). All studies to date rely on the assumption that

the traveltime residual can be linearly decomposed into a part corresponding to the 3-D velocity structure and a part for the topography, that is,

$$\delta t^{\text{measured}} = \delta t^{\text{3-D structure}} + \delta t^{\text{topo}} \quad (4)$$

We have all the tools to investigate whether precursor delay times can be analysed using such a linear assumption. Real data are measured with respect to PREM. In our case, the real earth corresponds to S20RTS+TOPO; therefore, $\delta t^{\text{measured}}$ corresponds to $\delta t^{[\text{S20RTS+TOPO}] - \text{PREM}}$. We then assume that we are able to make a perfect 3-D correction corresponding to $\delta t^{\text{3-D structure}} = \delta t^{\text{S20RTS-PREM}}$ and be left with $\delta t^{\text{topo}} = \delta t^{\text{S20RTS+TOPO}} - \delta t^{\text{S20RTS}}$. We can then define the following residual:

$$\delta t_{\text{residual}} = \delta t^{[\text{S20RTS+TOPO}] - \text{PREM}} - \delta t^{[\text{S20RTS+TOPO}] - \text{S20RTS}} - \delta t^{\text{S20RTS} - \text{PREM}} \quad (5)$$

If the delay times can be linearly decomposed, this residual should be identically zero. We measured the three contributions independently and show the results in Fig. 19 for the case of the ‘660’. We find that the residuals are as big as the data themselves. A similar result holds for the ‘410’. This leads to the conclusion that the traveltime data of the *SdS* precursors are not linearly decomposable and 3-D structure corrections for topography inferences based on linearised ray theory or finite-frequency in a single iteration cannot give correct results.

5 CONCLUSIONS

Our analysis showed that the interpretation of delay times of *SS* precursors using linearised ray theory can correctly identify the

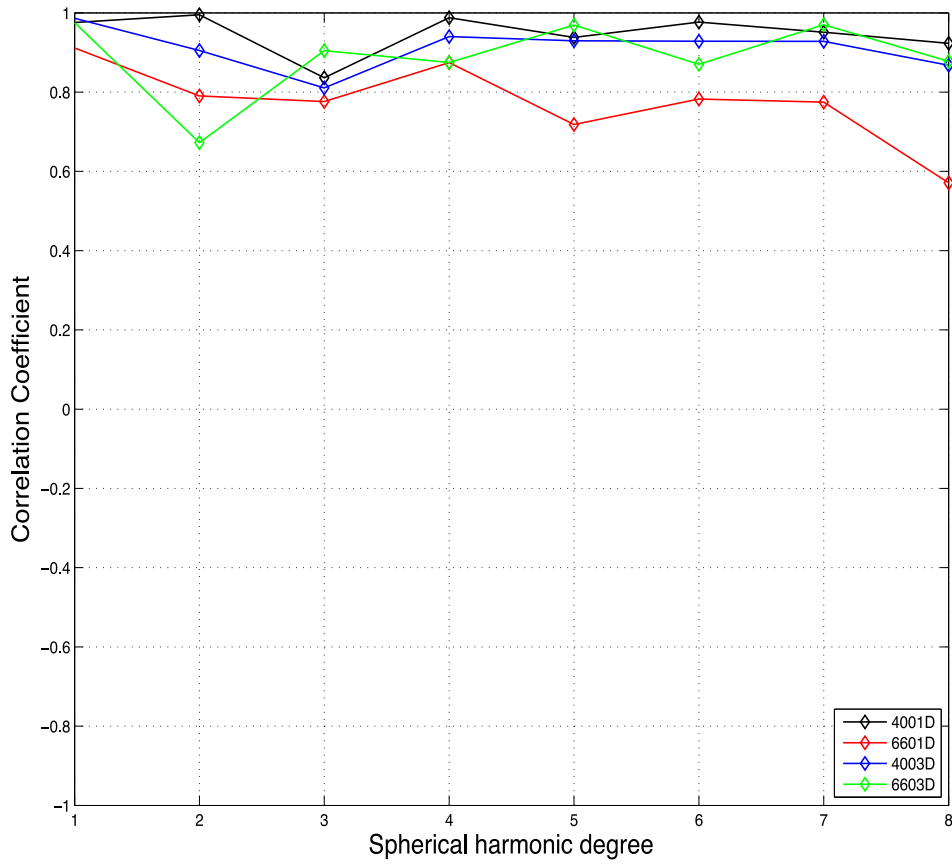


Figure 17. Correlation between inferred and input topography model as a function of spherical harmonic degree.

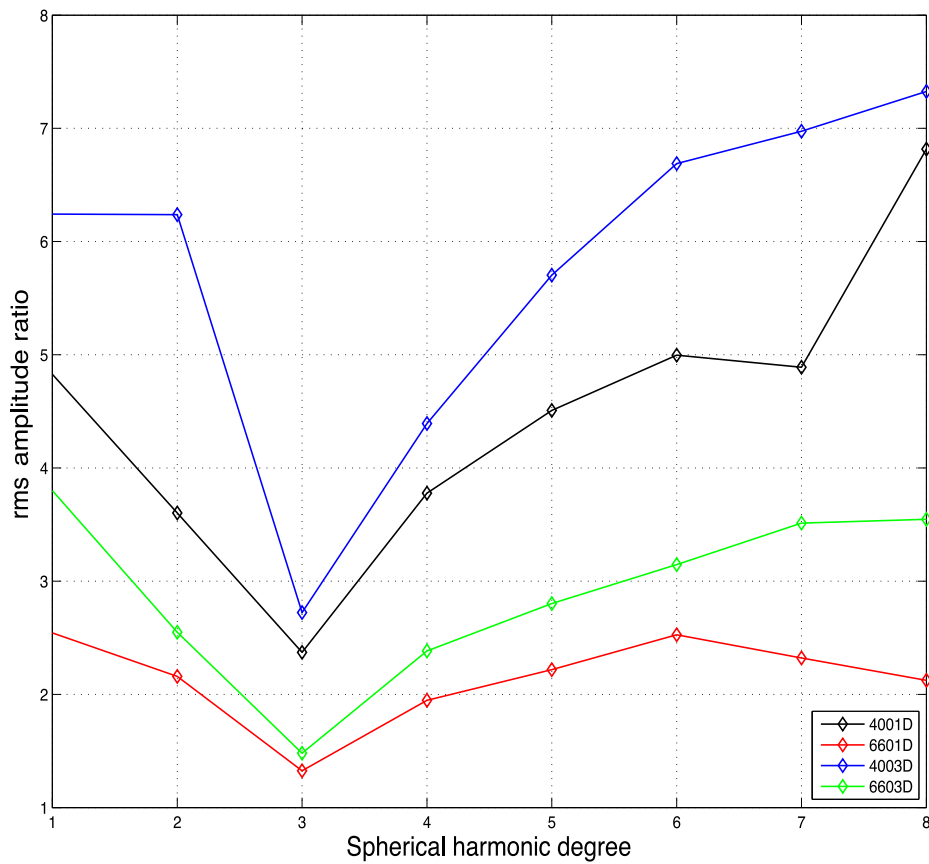


Figure 18. Rms amplitude ratio of input over inferred topography model as a function of spherical harmonic degree.

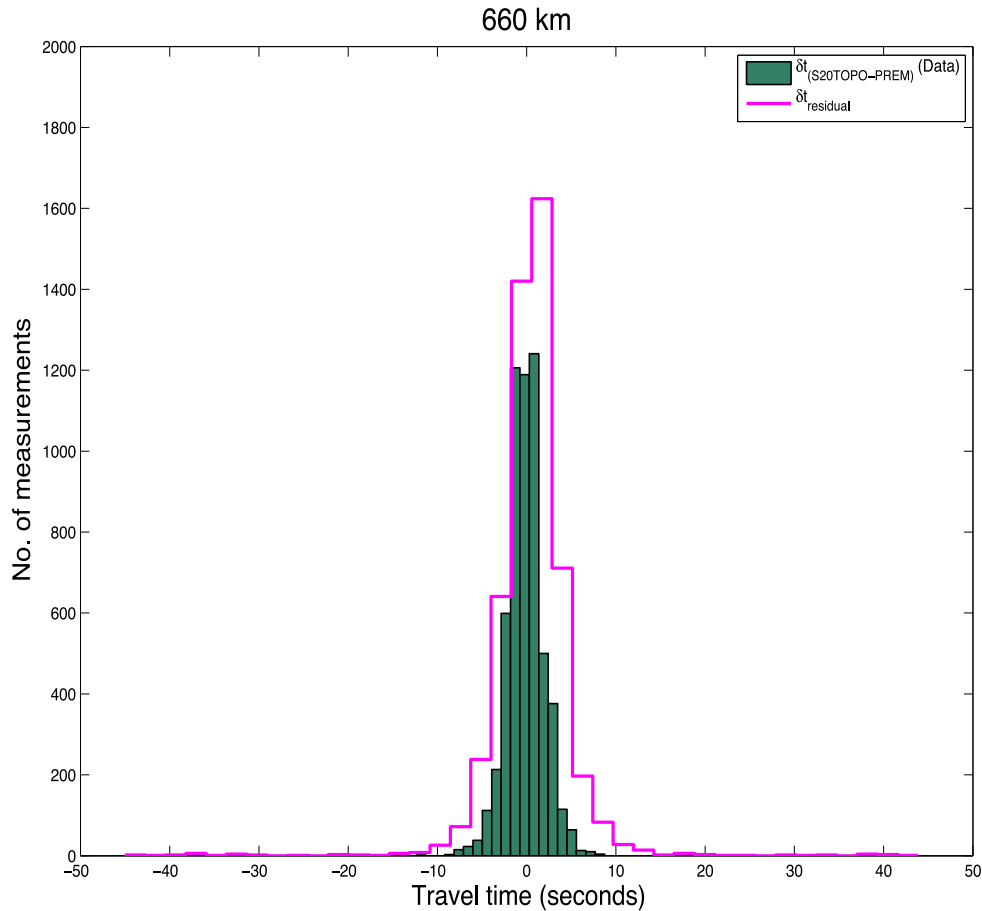


Figure 19. Histogram showing the distribution of the $\delta t_{\text{residual}}$ (purple line) and δt^{cc} (green bars). If the traveltime difference data were linear, $\delta t_{\text{residual}}$ would be close to zero, however, the corresponding histogram is wider than that for the data. The case shown is for the ‘660’ discontinuity.

positions of uplifts and depressions, provided that the bounce points are uniformly distributed. The amplitude of the topographic variations is severely underestimated. Even if the corrections for a 3-D velocity model are done perfectly, in a 3-D Earth, the inferences on topography are not as good as in a 1-D Earth model. We further conclude that the ‘660’ discontinuity distorts the waveforms so that the topography of the ‘410’ is not as easily inferred as that of the ‘660’. Our analysis of the *SS* delay times showed that they cannot be linearly decomposed into a 3-D velocity and a topography part, which means that linearised theories will never be able to invert for the topography in a single iteration. It is essential to infer the topography and the velocity structure together using a fully non-linear technique (ray theory or full waveform).

ACKNOWLEDGEMENTS

We thank Stephan Lessing and Jeroen Ritsema for constructive reviews. We further wish to thank Hanneke Paulssen and Arwen Deuss for useful discussions. The research leading to these results has received funding from the European Research Council under the European Union’s Seventh Framework Programme (FP/2007-2013)/ERC grant agreement no. 320639 (iGEO).

REFERENCES

Andrews, J. & Deuss, A., 2008. Detailed nature of the 660 km region of the mantle from global receiver function data, *J. geophys. Res.*, **113**, B06304, doi:10.1029/2007JB005111.

- Bai, L., Zhang, Y. & Ritsema, J., 2012. An analysis of *SS* precursors using spectral-element method seismograms, *Geophys. J. Int.*, **188**, 293–300.
- Bassin, C., Laske, G. & Masters, G., 2000. The current limits of resolution for surface wave tomography in North America, *EOS, Trans. Am. geophys. Un.*, **81**, F897.
- Chaljub, E. & Tarantola, A., 1997. Sensitivity of *SS* precursors to topography on the upper-mantle 660-km discontinuity, *Geophys. Res. Lett.*, **24**(21), 2613–2616.
- Chambers, K., Woodhouse, J.H. & Deuss, A., 2005. Topography of the 410-km discontinuity from *PP* and *SS* precursors, *Earth planet. Sci. Lett.*, **235**, 610–622.
- Chevrot, S., Vinnik, L. & Montagner, J.-P., 1999. Global-scale analysis of the mantle *Pds* phases, *J. geophys. Res.*, **104**(B9), 20 203–20 219.
- Crotwell, H.P., Owens, T.J. & Ritsema, J., 1999. The TauP Toolkit: flexible seismic travel-time and raypath utilities, *Seismol. Res. Lett.*, **70**, 154–160.
- Deuss, A., 2007. Seismic observations of transition-zone discontinuities beneath hotspot locations, *Geol. Soc. Am. Spec. Pap.*, **430**, 121–136.
- Deuss, A., 2009. Global observations of mantle discontinuities using *SS* and *PP* precursors, *Surv. Geophys.*, **30**, 301–326.
- Deuss, A. & Woodhouse, J.H., 2002. A systematic search for mantle discontinuities using *SS*-precursors, *Geophys. Res. Lett.*, **29**(8), 90-1–90-4.
- Dziewoński, A.M. & Anderson, D.L., 1981. Preliminary reference Earth model, *Phys. Earth planet. Inter.*, **25**, 297–356.
- Eagar, K.C., Fouch, M.J. & James, D.E., 2010. Receiver function imaging of upper mantle complexity beneath the Pacific Northwest, United States, *Earth planet. Sci. Lett.*, **297**, 141–153.
- Estabrook, C.H. & Kind, R., 1996. The nature of the 660-kilometer upper-mantle seismic discontinuity from precursors to the *PP* phase, *Science*, **274**(5290), 1179–1182.

- Flanagan, M. & Shearer, P., 1998. Global mapping of topography on transition zone velocity discontinuities by stacking *SS* precursors, *J. geophys. Res.*, **103**, 2673–2692.
- Flanagan, M. & Shearer, P., 1999. A map of topography of 410-km discontinuity from *PP* precursors, *Geophys. Res. Lett.*, **26**(5), 549–552.
- Gu, Y.J. & Dziewonski, A.M., 2002. Global variability of transition zone thickness, *J. geophys. Res.*, **107**(B7), 2135, doi:10.1029/2001JB000489.
- Gu, Y.J., Dziewonski, A.M. & Ekström, G., 2003. Simultaneous inversion for mantle shear velocity and topography of transition zone discontinuities, *Geophys. J. Int.*, **154**, 559–583.
- Houser, C., Masters, G., Flanagan, M. & Shearer, P., 2008. Determination and analysis of long-wavelength transition zone structure using *SS* precursors, *Geophys. J. Int.*, **174**, 178–194.
- Komatitsch, D. & Tromp, J., 1999. Introduction to the spectral-element method for 3-D seismic wave propagation, *Geophys. J. Int.*, **139**(3), 806–822.
- Komatitsch, D. & Tromp, J., 2002a. Spectral-element simulations of global seismic wave propagation-I. Validation, *Geophys. J. Int.*, **149**(2), 390–412.
- Komatitsch, D. & Tromp, J., 2002b. Spectral-element simulations of global seismic wave propagation-II. 3-D models, oceans, rotation, and self-gravitation, *Geophys. J. Int.*, **150**(1), 303–318.
- Komatitsch, D. & Vilotte, J.P., 1998. The spectral-element method: an efficient tool to simulate the seismic response of 2D and 3D geological structures, *Bull. seism. Soc. Am.*, **88**(2), 368–392.
- Kustowski, B., Ekström, G. & Dziewonski, A.M., 2008. Anisotropic shear-wave velocity structure of the Earth's mantle: a global model, *J. geophys. Res.*, **113**(B6), B06306, doi:10.1029/2007JB005169.
- Lawrence, J.F. & Shearer, P.M., 2006. A global study of transition zone thickness using receiver functions, *J. geophys. Res.*, **111**, B06307, doi:10.1029/2005JB003973.
- Lawrence, J.F. & Shearer, P.M., 2008. Imaging mantle transition zone thickness with *SdS-SS* finite-frequency sensitivity kernels, *Geophys. J. Int.*, **174**, 143–158.
- Lessing, S., Thomas, C., Rost, S., Cobden, L. & Dobson, D., 2014. Mantle transition zone structure beneath India and western China from migration of *PP* and *SS* precursors, *Geophys. J. Int.*, **197**, 396–413.
- Meier, U., Trampert, J. & Curtis, A., 2009. Global variations of temperature and water content in the mantle transition zone from higher mode surface waves, *Earth planet. Sci. Lett.*, **282**, 91–101.
- Morgan, J.P. & Shearer, P., 1993. Seismic constraints on mantle flow and topography of the 660-km discontinuity: evidence for whole mantle convection, *Nature*, **365**, 506–511.
- Neele, F., de Regt, H. & VanDecar, J., 1997. Gross errors in upper-mantle discontinuity topography from underside reflection data, *Geophys. J. Int.*, **129**, 194–204.
- Paulssen, H., 1988. Evidence for a sharp 670-km discontinuity as inferred from *P*-to-*S* converted waves, *J. geophys. Res.*, **93**, 10 489–10 500.
- Ritsema, J., Van Heijst, H.J. & Woodhouse, J.H., 1999. Complex shear velocity structure imaged beneath Africa and Iceland, *Science*, **286**, 1925–1928.
- Schmerr, N. & Garnero, E., 2006. Investigation of upper mantle discontinuity structure beneath the central Pacific using *SS* precursors, *J. geophys. Res.*, **111**, B08305, doi:10.1029/2005JB004197.
- Schmerr, N. & Garnero, E., 2007. Upper mantle discontinuity topography from thermal and chemical heterogeneity, *Science*, **318**(5850), 623–626.
- Schultz, R. & Gu, Y., 2013. Multiresolution imaging of mantle reflectivity structure using *SS* and *P'P'* precursors, *Geophys. J. Int.*, **195**, 668–683.
- Shearer, P.M., 1991. Constraints on upper mantle discontinuities from observations of long-period reflected and converted phases, *J. geophys. Res.*, **96**, 18 147–18 182.
- Shearer, P., 1993. Global mapping of upper mantle reflectors from long-period *SS* precursors, *Geophys. J. Int.*, **115**, 878–904.
- Shearer, P.M., 2000. Upper mantle seismic discontinuities, in *Earth's Deep Interior: Mineral Physics and Tomography from the Atomic to the Global scale*, Geophysical Monograph, vol. 117, pp. 115–131, American Geophysical Union.
- Shearer, P. & Masters, G., 1992. Global mapping of topography on 660-km discontinuity, *Nature*, **355**, 791–796.
- Shearer, P., Flanagan, M.P. & Hedin, A., 1999. Experiments in migration processing of *SS* precursor data to image upper mantle discontinuity structure, *J. geophys. Res.*, **104**, 7229–7242.
- Tauzin, B., Debayle, E. & Wittlinger, G., 2008. The mantle transition zone as seen by global *Pds* phases: no clear evidence for a thin transition zone beneath hotspots, *J. geophys. Res.*, **113**, B08309, doi:10.1029/2007JB005364.
- Tauzin, B., van der Hilst, R., Wittlinger, G. & Ricard, Y., 2013. Multiple transition zone seismic discontinuities and low velocity layers below western United States, *J. geophys. Res.*, **118**, 2307–2322.
- Thomas, C. & Billen, M.I., 2009. Mantle transition zone structure along a profile in the SW Pacific: thermal and compositional variations, *Geophys. J. Int.*, **176**(1), 113–125.
- Tonegawa, T., Hirahara, K. & Shibutani, T., 2005. Detailed structure of the upper mantle discontinuities around the Japan subduction zone imaged by receiver function analyses, *Earth Planets Space*, **57**, 5–14.
- Trampert, J. & Snieder, R., 1996. Model Estimations by truncated expansions: possible artifacts in seismic tomography, *Science*, **271**, 1257–1260.
- Vasco, D.W., Johnson, L.R. & Pulliam, J., 1995. Lateral variations in mantle velocity structure and discontinuities determined from *P*, *PP*, *S*, *SS*, and *SS-SdS* travel time residuals, *J. geophys. Res.*, **100**, 24 037–24 059.
- Zhao, L. & Chevrot, S., 2003. *SS*-wave sensitivity to upper mantle structure: implications for the mapping of transition zone discontinuity topographies, *Geophys. Res. Lett.*, **30**(11), 1590, doi:10.1029/2003GL017223.
- Zheng, Z., Ventosa, S. & Romanowicz, B., 2015. High resolution upper mantle discontinuity images across the Pacific Ocean from *SS* precursors using local slant stack filters, *Geophys. J. Int.*, **202**, 175–189.